

# Parallel Stitching of 2D Materials

Xi Ling, Yuxuan Lin, Qiong Ma, Ziqiang Wang, Yi Song, Lili Yu, Shengxi Huang, Wenjing Fang, Xu Zhang, Allen L. Hsu, Yaqing Bie, Yi-Hsien Lee, Yimei Zhu, Lijun Wu, Ju Li, Pablo Jarillo-Herrero, Mildred Dresselhaus, Tomás Palacios,\* and Jing Kong\*

As the fundamental limit of Moore's law is approaching, the global semiconductor industry is intensively looking for applications beyond complementary metal-oxide semiconductor (CMOS) electronics.<sup>[1]</sup> The atomically thin and ultraflexible nature of two-dimensional (2D) materials (such as graphene, hexagonal boron nitride (hBN), and transition-metal dichalcogenides (TMDs)) offer a competitive solution not only to push the forefront of semiconductor technology further, toward or perhaps beyond the Moore's law, but also to potentially realize a new vision of ubiquitous electronics and optoelectronics in the near future.<sup>[2,3]</sup> Hybrid structures between 2D materials are essential building blocks with multifunctionality and broader capacity for nanoscale modern electronics and optoelectronics.<sup>[4–10]</sup> The stacking of van der Waals heterostructures in the vertical direction can be accomplished by either mechanical transfer or heteroepitaxy,<sup>[4–6,8,9]</sup> whereas atomic stitching of 2D materials in the horizontal direction through conventional nanofabrication technology has proven to be far more challenging, mainly because of the lack of a selective etching method for each specific 2D material. Precise spatial control and self-limiting processes are highly desired to design and

prepare lateral heterostructures. Researchers have attempted to build lateral heterostructures between materials with similar lattice structures and small lattice mismatch, such as graphene–hBN and TMD–TMD lateral heterostructures.<sup>[4,10–16]</sup> However, a parallel connection between two atomic layers with significant crystallographic dissimilarity, such as graphene–TMD or hBN–TMD lateral heterostructures, has never been achieved. Furthermore, most of these methods are not suitable for large-scale production.

Here, we report a general synthesis methodology to achieve in-plane “parallel stitched” heterostructures between 2D and TMD materials regardless of the lattice mismatch between materials, with large-scale production capability. This enables both multifunctional electronic/optoelectronic devices and their large scale integration. In this method, during the chemical vapor deposition (CVD) of TMDs,<sup>[16]</sup> aromatic molecules, which are used as seeds to facilitate the growth, can be “sowed” either on the substrate or on another pre-deposited 2D material, in which the “sowing” process is selective depending on the wettability of the seeds and surfaces. Consequently, parallel stitched or vertically stacked<sup>[17]</sup> heterostructures between TMDs and diverse 2D materials can be achieved regardless of lattice mismatch between materials. This technique offers an opportunity to synthesize many basic functional building blocks for electronic and optoelectronic devices in 2D, including metal–semiconductor (e.g., graphene–MoS<sub>2</sub>), semiconductor–semiconductor (e.g., WS<sub>2</sub>–MoS<sub>2</sub>), and insulator–semiconductor (e.g., hBN–MoS<sub>2</sub>) heterostructures. Large-scale parallel stitched graphene–MoS<sub>2</sub> heterostructures were further investigated. Unique nanometer overlapped junctions were obtained at the parallel stitched interface, which are highly desirable both as metal–semiconductor contact and functional devices/systems, such as for use in logical integrated circuits (ICs).

**Figure 1a** illustrates the growth procedure of the parallel stitched heterostructure between a TMD and another 2D material through the selective “sowing” of perylene-3,4,9,10-tetracarboxylic acid tetrapotassium salt (PTAS) molecules on the growth substrate. The details are given in the Experimental Section and Section S1 of the Supporting Information. The first 2D material is transferred onto a SiO<sub>2</sub>/Si substrate (growth substrate) and can be patterned by lithography and etching. PTAS molecules were deposited onto a substrate (seed reservoir) placed next to the growth substrate. At the elevated growth temperature in the presence of a carrier gas, the PTAS molecules reach the growth substrate. From our studies, it was observed that PTAS is more likely to be deposited onto a hydrophilic surface (SiO<sub>2</sub>) rather than on the surfaces of 2D materials, which are mostly hydrophobic.<sup>[18,19]</sup> PTAS molecules are therefore “sowed” only in the regions without the first 2D material. This promotes the growth

Dr. X. Ling, Y. Lin, Y. Song, L. Yu, S. Huang, W. Fang,  
X. Zhang, Dr. A. L. Hsu, Prof. M. Dresselhaus,  
Prof. T. Palacios, Prof. J. Kong  
Department of Electrical Engineering and  
Computer Science  
Massachusetts Institute of Technology  
Cambridge, MA 02139, USA  
E-mail: tpalacios@mit.edu; jingkong@mit.edu



Q. Ma, Dr. Y. Bie, Prof. P. Jarillo-Herrero, Prof. M. Dresselhaus  
Department of Physics  
Massachusetts Institute of Technology  
Cambridge, MA 02139, USA

Z. Wang, Prof. J. Li  
Department of Materials Science and Engineering  
Massachusetts Institute of Technology  
Cambridge, MA 02139, USA

Prof. Y.-H. Lee  
Materials Science and Engineering  
National Tsing-Hua University  
Hsinchu 30013, Taiwan

Dr. Y. Zhu, Dr. L. Wu  
Condensed Matter Physics and Materials Science Department  
Brookhaven National Laboratory  
Upton, NY 11973, USA

Prof. J. Li  
Department of Nuclear Science and Engineering  
Massachusetts Institute of Technology  
Cambridge, MA 02139, USA

DOI: 10.1002/adma.201505070

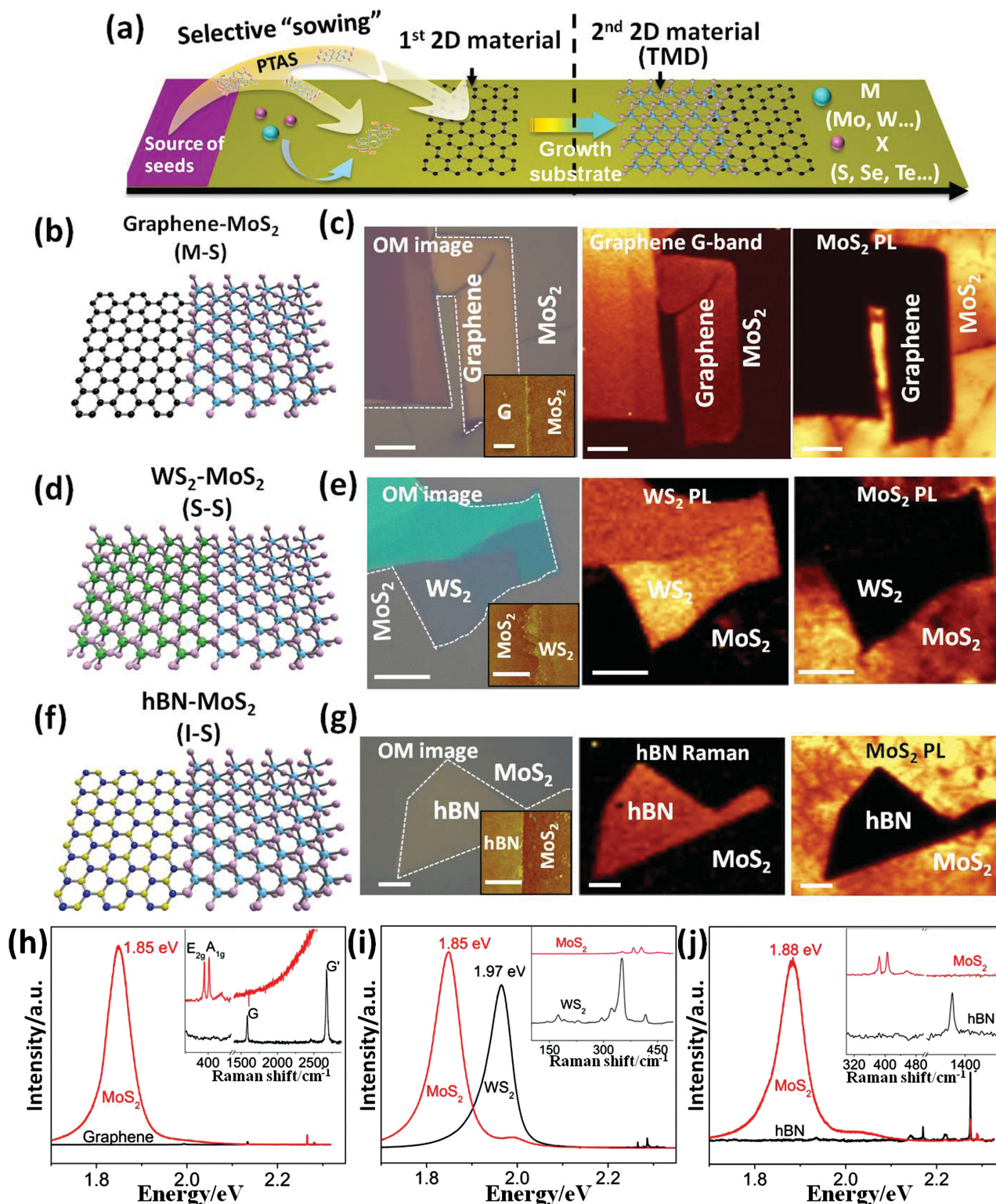


**Figure 1.** Diverse parallel stitched heterostructures between MoS<sub>2</sub> and various 2D materials. a) Schematic illustration of the CVD setup and the process for synthesis of the parallel stitched 2D-TMD heterostructure. b,d,f) Schematic illustration of the parallel stitched heterostructures of graphene-MoS<sub>2</sub> (b), WS<sub>2</sub>-MoS<sub>2</sub> (d), and hBN-MoS<sub>2</sub> (f). c,e,g) Typical optical images, spectroscopy intensity mapping images of the structures corresponding to (b), (d), and (f). The boundaries between MoS<sub>2</sub> and the pre-existing 2D materials are marked by the white dashed line. The scale bars are 5 μm. The insets in the optical images are the AFM images of the heterojunction (the scale bars are 500 nm). h-j) Typical PL spectra and Raman spectra (insets) collected on MoS<sub>2</sub> and the pre-existing 2D materials areas of the parallel stitched heterostructures (h) of WS<sub>2</sub>-MoS<sub>2</sub> (i) and hBN-MoS<sub>2</sub> (j).



of the second 2D material (TMD) within the  $\text{SiO}_2$  region with abundant seed molecules, whereas there is very limited TMD growth in the first 2D material region, due to the negligible amount of seed molecules. Consequently, the growth of the second 2D material only occurs in the  $\text{SiO}_2$  regions, allowing the formation of parallel stitched heterostructures along the edges of the first 2D material.

Figure 1b–j shows the growth results of the parallel stitched heterostructures of graphene– $\text{MoS}_2$ ,  $\text{WS}_2$ – $\text{MoS}_2$ , and hBN– $\text{MoS}_2$  as the prototypes of metal–semiconductor (M–S), semiconductor–semiconductor (S–S), and insulator–semiconductor (I–S) heterostructures, respectively. Optical microscopy, atomic force microscopy (AFM) (insets in Figure 1c,e,g and Figure S2, Supporting Information), and spectroscopy characterizations (Figure 1h–j) were carried out. These studies reveal that high quality  $\text{MoS}_2$  is grown on the exposed  $\text{SiO}_2$  regions, not on top of the first 2D materials, but are well connected with them at the edges with minimal overlaps. The photoluminescence (PL) and Raman spectra are collected on and outside the first 2D materials, as shown in Figure 1h–j. The intense PL signal

$\approx 1.85$  eV, and the  $E_{2g}$  and  $A_{1g}$  Raman modes ( $\Delta\omega = 21$   $\text{cm}^{-1}$ ) obtained in the  $\text{MoS}_2$  region (red traces in Figure 1h–j) indicates the high quality of the monolayer  $\text{MoS}_2$ .<sup>[17]</sup> While on top of the first 2D materials (black traces in Figure 1h–j), only the Raman modes from them (monolayer graphene: G-band at  $1582$   $\text{cm}^{-1}$  and G'-band at  $2676$   $\text{cm}^{-1}$ ;  $\text{WS}_2$ : 174, 295, 322, 350, and  $417$   $\text{cm}^{-1}$ ; hBN:  $1368$   $\text{cm}^{-1}$ ) were observed. The intensity mappings of the Raman (or PL) signals from the first 2D materials and the PL from  $\text{MoS}_2$  further indicate that high-quality monolayer  $\text{MoS}_2$  was only grown outside the first 2D materials (Figure 1c,e,g). We consequently conclude that sharp and well-stitched boundaries were formed at the edges of the first 2D materials, with no breaks or tears.

Since there is a large lattice mismatch (25%) between graphene and  $\text{MoS}_2$ , the epitaxial growth between graphene and  $\text{MoS}_2$  is, in principle, more difficult than that between graphene and hBN,<sup>[12]</sup> or between two different TMDs.<sup>[14–16]</sup> High-resolution transmission electron microscopy (HRTEM) was therefore carried out on the graphene– $\text{MoS}_2$  parallel stitched heterostructures for structural characterization (Figure 2a,b).

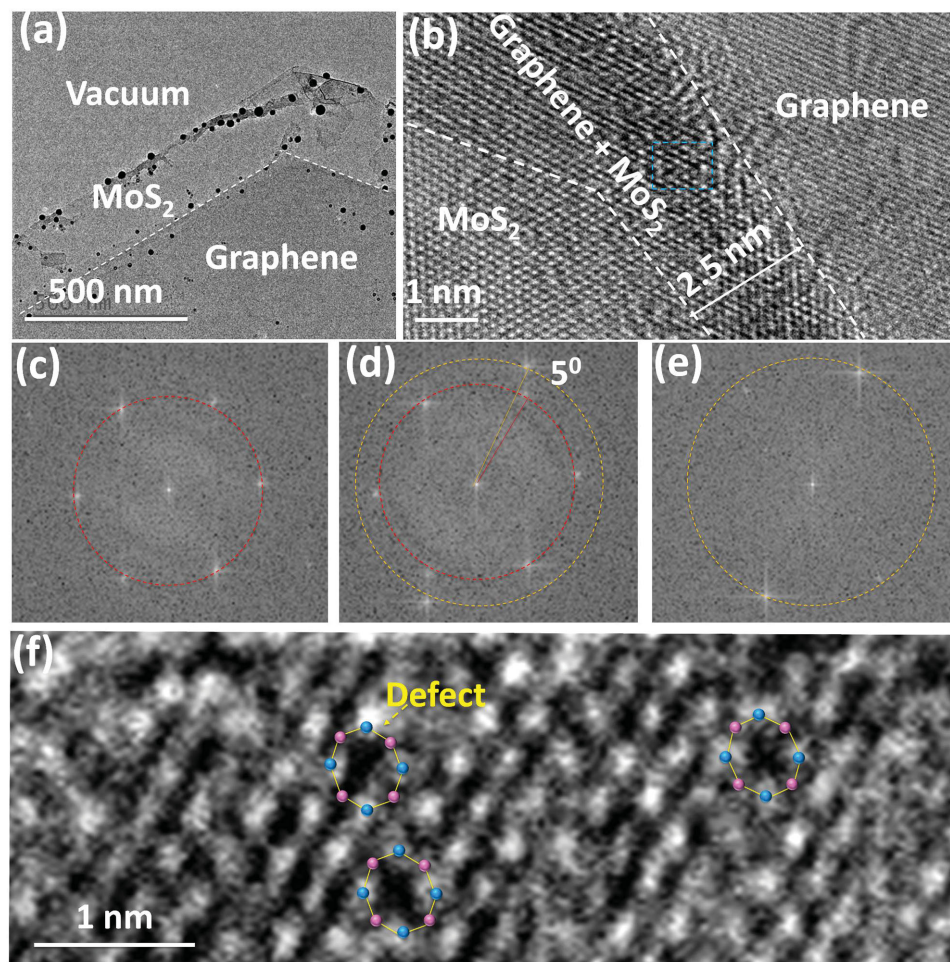


**Figure 2.** TEM characterizations of the parallel stitched graphene– $\text{MoS}_2$  heterojunction. a) Low-magnification bright-field TEM image showing the graphene– $\text{MoS}_2$  interface. b) HRTEM image showing the atom arrangement at the graphene– $\text{MoS}_2$  heterojunction with the size of the overlapping region of 2.5 nm. c–e) Diffraction patterns corresponding to the  $\text{MoS}_2$  region (c), the graphene– $\text{MoS}_2$  overlapping region (d), and the graphene region (e). The red and orange circles mark the diffraction patterns from  $\text{MoS}_2$  and graphene, respectively. f) Zoomed-in HRTEM image of the graphene– $\text{MoS}_2$  overlapping area marked by blue in (b) showing the eight-member rings defects.

Selected-area TEM diffractograms indicate that the dark area between the dashed lines in Figure 2b consists of graphene and MoS<sub>2</sub>, while only MoS<sub>2</sub> (left side) or graphene (right side) can be observed outside the interface region. This indicates that MoS<sub>2</sub> overlaps with graphene at the boundary between them. The width of most of the overlapping region is 2–30 nm (Figure 2b and Figure S4, Supporting Information). Figure 2b shows a heterojunction with an overlap region of only 2.5 nm wide. The atomic structures are clearly seen on the MoS<sub>2</sub>, graphene, and overlapping regions (Figure 2b and Figure S5, Supporting Information). Figure 2c–e shows the diffractograms through fast Fourier transform (FFT) in each of these three regions. The red circle marks the diffraction pattern from the MoS<sub>2</sub> lattice structure with a spacing of 2.7 Å corresponding to the (100) planes. The orange circle marks the 2.1 Å spacing from the (110) planes of the graphene lattice structure. The FFT diffraction pattern of the overlapping region indicates that there is a 5° rotation angle between the MoS<sub>2</sub> and graphene lattices. Comparing Figure 2d with Figure 2c,e, the corresponding MoS<sub>2</sub> and graphene lattice spacing individually remain at 2.7 and 2.1 Å, respectively, in the overlapping region, indicating that there is no lattice distortion at their interface. As the lattice mismatch between MoS<sub>2</sub> and graphene is relatively large, the unchanged lattice constants for both of them at the interface indicate that MoS<sub>2</sub> and graphene are connected with each other

presumably through a van der Waals interaction. A similar analysis was done on more samples, showing that the rotation angles between the two materials are all within a small range of 0–10° (Figure S4, Supporting Information).

A closer look reveals more atomic defects in the overlapping region (Figure 2f) than that in the regions away from the interface. There are mainly two kinds of defects in the MoS<sub>2</sub> lattice: Mo–Mo bond defects and –S– bridge defects.<sup>[20,21]</sup> The –S– bridge defect looks like an eight-member ring in the lattice, while the Mo–Mo bond defect corresponds to a 4+8-member ring. Both defects have been observed at MoS<sub>2</sub> grain boundaries.<sup>[21]</sup> In the overlapping regions of the lateral structures, however, the MoS<sub>2</sub> defects are mainly eight-member ring defects, as marked in the Figure 2f, suggesting that the absence of seed molecules on graphene is related to a lack of sulfur for the MoS<sub>2</sub> growth. Possibly, the increased density of defects at the interface results in the inhibition of MoS<sub>2</sub> growth further into the graphene region.

One unique advantage of the parallel stitching method is that it enables large scale integration. Here, we demonstrate the construction of many graphene–MoS<sub>2</sub> parallel stitched heterostructures with arbitrary patterns (Figure 3 and Figure S6, Supporting Information). Figure 3 shows the typical optical images and spectroscopy characterization of a parallel stitched graphene–MoS<sub>2</sub> heterostructure array (Figure 3a–c), the logo

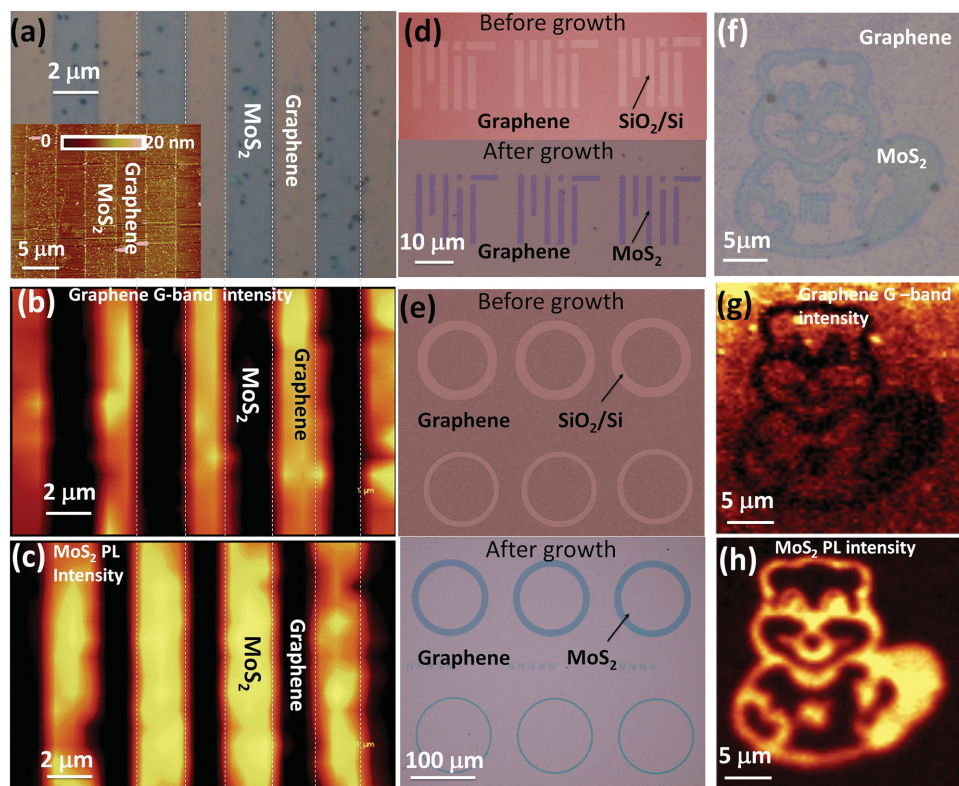


**Figure 3.** Demonstration of the parallel stitched graphene–MoS<sub>2</sub> heterojunction in a large scale with arbitrary patterns. Typical optical images of a) the graphene–MoS<sub>2</sub> periodic array, b) the corresponding mapping image of G-band intensity of graphene, and c) PL intensity of MoS<sub>2</sub>. The inset in (a) shows the typical AFM image of graphene–MoS<sub>2</sub> periodic array. d,e) Optical images before (top) and after (bottom) MoS<sub>2</sub> grown on patterned graphene pattern with the “MIT” logo (d) and rings (e). f) Optical image of a MoS<sub>2</sub>-filled MIT mascot “Tim the beaver” on a graphene pattern. g,h) The corresponding mapping images of G-band intensity of graphene (g), and PL intensity of MoS<sub>2</sub> (h).



of Massachusetts Institute of Technology (MIT) (Figure 3d and Figure S6, Supporting Information), rings (Figure 3e), and MIT mascot “Tim the Beaver” (Figure 3f–h). It is observed that the mapping images of the G-band Raman intensity from graphene (Figure 3b,g) and PL intensity from MoS<sub>2</sub> (Figure 3c,h) are highly correlated with each other and match well with the corresponding optical image (Figure 3a,f). The AFM image in the inset in Figure 3a indicates that the periodic heterostructures are well connected with very narrow overlaps at the interfaces. These morphological and spectroscopic measurement results give further evidence that the MoS<sub>2</sub> and graphene are separated in space and stitched together at the edges. Using this method, one can design graphene–MoS<sub>2</sub> heterojunctions at will. As shown by the MoS<sub>2</sub>-filled MIT mascot “Tim the Beaver” (Figure 3f–h), the spatial resolution of the MoS<sub>2</sub> patterns in the images can be as low as 1  $\mu\text{m}$  (limited by the spatial resolution of the spectrometer). The geometrical flexibility, good controllability, and large-scale fabrication capability offer great opportunity for 2D hybrid multifunctional applications.

Transport measurements across graphene–MoS<sub>2</sub> parallel stitched heterojunctions indicate that a weak tunneling barrier forms at the junction. The inset in Figure 4a shows an optical image of the device. As shown in Figure 4a, both the reverse-bias current (when  $V_j < 0$ ) and the forward-bias current (when  $V_j > 0$ ) increase superlinearly with the junction voltage. This behavior is an indication that a tunneling barrier is present.<sup>[22–24]</sup> Figure 4b shows the measured barrier height ( $\Phi_B$ ) at the junction (from temperature-dependent measurements (Figure S7, Supporting Information) as a function of gate voltage, the barrier height is extracted to be  $\approx 70$  meV at zero gate voltage and less than 20 meV at high positive gate voltage ( $V_G > 30$  V), which is similar to that for the graphene–MoS<sub>2</sub> vertically stacked heterostructure.<sup>[25]</sup> The junction resistance ( $R_j = V_j/I_j$ ) is  $\approx 0.3$  k $\Omega$  mm when MoS<sub>2</sub> is turned on ( $V_G = 30$  V). Recent works have shown that graphene–MoS<sub>2</sub> vertically stacked heterostructures, when used as contacts to MoS<sub>2</sub> channels, can lead to a much lower contact resistance than conventional metal contacts.<sup>[22,25,26]</sup> However, the vertically stacked structures would suffer from various problems when the MoS<sub>2</sub> transistors are scaled down to nanometer scale, such as: i) difficulty in alignment with a high spatial resolution, ii) the lack of a selective etching technique, and iii) the large parasitic impedances. In contrast, the parallel stitched junctions grown with the method presented here can serve as a self-aligned lateral Ohmic contact to the MoS<sub>2</sub> channel. Such contact has been referred to as 1D contact<sup>[27]</sup> and has been shown to be able to address these problems very well without degrading the contact quality. Implementing these 1D contacts has previously been a tremendous challenging task,<sup>[27]</sup> but can be simply realized with our selective “sowing” method here.

Using graphene–MoS<sub>2</sub> parallel stitched heterostructures as the source/drain contacts of top-gated MoS<sub>2</sub> transistors (Figure S8, Supporting Information), we fabricated arrays of the basic building blocks of integrated circuits (shown in Figure 4c–j). Figure 4d shows the microscopic image and the transistor-level schematic of a diode-connected MoS<sub>2</sub> transistor, indicating good rectifying behavior, with an on–off current ratio on the order of  $10^6$ , obtained according to the

I–V characteristics in Figure 4e. Based on the direct-coupled transistor logic technology,<sup>[28]</sup> which has been widely used in high-speed logic circuits with low power consumption, we successfully fabricated inverter (Figure 4f,g,h) and negative-AND (NAND) gates (Figure 4i,j), which are a complete set of logic circuits and can, in principle, realize any two-level combinational logics. Figure 4f plots the typical voltage transfer characteristics of an inverter, with the power-supply voltage ( $V_{dd}$ ) ranging from 3 to 6 V, with a full logic swing and a symmetric and abrupt on–off transition. The voltage gain, given by  $A_v = dV_{out}/dV_{in}$ , as shown in the inset of Figure 4f, has a sharp peak at the medium voltage level ( $V_{dd}/2$ ), with a value up to 7. This, together with the well-matched input–output range, guarantees the normal operation when multiple stages of logic gates are cascaded. Figure 4h,j shows the transient responses of an inverter and a NAND gate, respectively, in which the output voltage of the inverter is always the opposite of the input voltage, and the output voltage of the NAND gate is “low” only when both its inputs are “high.” Note that the propagation delay of our logic gates still needs further improvement. This is just a proof of concept demonstration, and further optimizations will be made, such as resizing the transistor, work function matching,<sup>[28]</sup> etc., to address the optimization issue.

In summary, as conventional lithography/selective etching is incapable for use in the large scale integration of 2D materials to achieve various junctions for future electronics and optoelectronics, in this work a universal methodology is proposed to address such challenges. By introducing the selective “sowing” of the molecules as seeds at different positions on a growth substrate during the synthesis of monolayer TMD materials, in-plane heterojunctions of TMD with other 2D materials can be constructed. The method of heterojunction formation is effective, simple, and powerful, not only offering solutions for large-scale 2D materials integration but also enabling development of versatile parallel stitched in-plane junctions which are unique in structure and properties, thus offering tremendous potential, as demonstrated through the example of large-scale manufacturing of parallel stitched graphene–MoS<sub>2</sub> heterostructures and the investigation of their potential applications.

## Experimental Section

**Heterostructure Growth:** In this work, graphene was prepared by either mechanical exfoliation or CVD growth and transferred onto a cleaned 300 nm SiO<sub>2</sub>/Si substrate. Other 2D materials (WS<sub>2</sub> and hBN) were prepared by mechanical exfoliation. For the parallel stitched heterostructures between MoS<sub>2</sub> and other 2D materials, PTAS molecules were used as seeds. The growth substrate (SiO<sub>2</sub>/Si wafer with the first 2D material, preannealed at 380  $^{\circ}\text{C}$  for 2 h with 200 sccm Ar/200 sccm H<sub>2</sub> gas flow as protection) was suspended between two SiO<sub>2</sub>/Si substrates with abundant PTAS as the seed reservoir, as shown in Figure S1 (Supporting Information). All of these substrates were faced down and placed in a crucible containing a molybdenum oxide (MoO<sub>3</sub>) precursor. This crucible was put in the middle of a 1 inch quartz tube reaction chamber, with another sulfur (S) containing crucible upstream in the quartz tube. Before heating, the whole CVD system was purged with 1000 sccm Ar (99.999% purity) for 3 min. Then, 5 sccm Ar was introduced into the system as a carrier gas. The system was heated to 650  $^{\circ}\text{C}$  at a rate of 15  $^{\circ}\text{C min}^{-1}$ , and MoS<sub>2</sub> was synthesized at 650  $^{\circ}\text{C}$

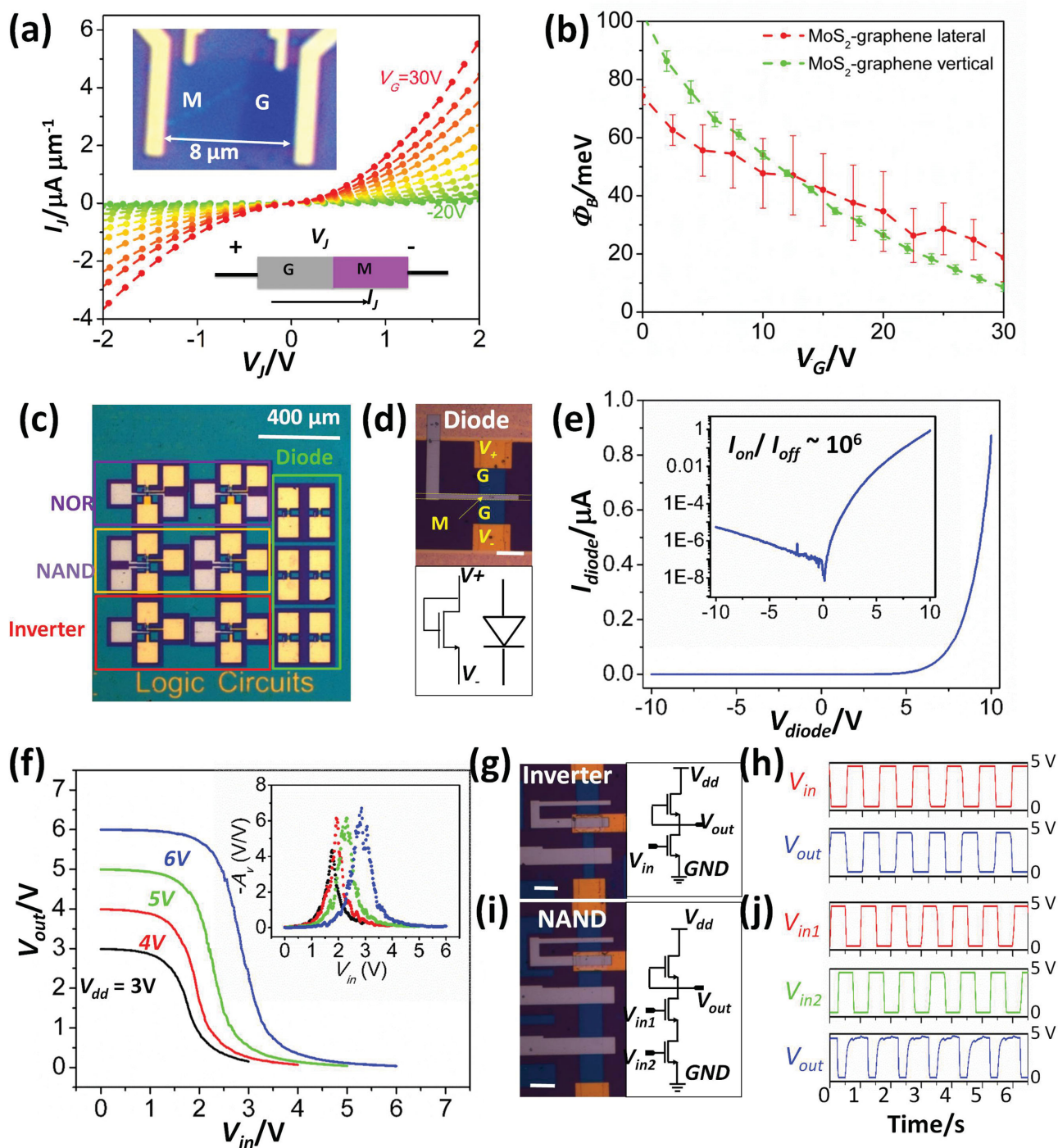


**Figure 4.** Transport measurement results and large-scale integrated circuit applications of the parallel stitched graphene–MoS<sub>2</sub> heterojunction. a) Output characteristics of the graphene–MoS<sub>2</sub> heterojunction with different gate bias from –20 to 30 V with 5 V intervals. Upper inset: Microscopic image of the four-probe graphene–MoS<sub>2</sub> heterojunction device on top of 300 nm SiO<sub>2</sub> as the back gate dielectric. Lower inset: Schematic of the device with graphene (G) as the positive side and MoS<sub>2</sub> (M) as the negative side of the junction. b) The barrier height at the lateral (red) and vertical (green) graphene–MoS<sub>2</sub> heterojunctions as a function of the gate voltage. c) Microscopy image of the test chip of the logic circuit arrays based on the parallel stitched graphene–MoS<sub>2</sub> heterojunctions. d,g,i) Microscopy images and transistor-level schematics of the diode-connected transistor (d), the inverter (g), and the NAND gate (i). Scale bar: 10 μm. e) *I*–*V* characteristics of the diode-connected transistor. Inset: *I*–*V* characteristic of the diode on a log scale. The on–off ratio is ≈10<sup>6</sup>. f) The voltage transfer characteristics of the inverter, with the power supply voltage (*V*<sub>dd</sub>) from 3 to 6 V. Inset: The corresponding voltage gain (*A*<sub>v</sub> = d*V*<sub>out</sub>/d*V*<sub>in</sub>) of the inverter. h,j) Transient response of the inverter (h) and the NAND gate (j).

for 3 min under atmospheric pressure. The temperature at the position where the sulfur was located was set to be  $\approx 180^\circ\text{C}$  during growth. The system was finally cooled down to room temperature quickly by opening the furnace and taking out the quartz tube, and 1000 sccm Ar flow was used to remove the reactants.

**TEM Characterization:** An as-grown graphene–MoS<sub>2</sub> heterostructure was transferred onto a TEM grid (Quantifoil, No. 656-200-CU, TED PELLA, INC.) by the poly(methyl methacrylate) (PMMA) method.<sup>[21]</sup> After transfer onto a TEM grid, the PMMA was removed under vacuum annealing at  $350^\circ\text{C}$  for half an hour. HRTEM characterization of the heterostructure at the atomic scale was carried out with a JOEL ARM 200CF TEM equipped with a cold field-emission electron source and two spherical-aberration correctors operated under an accelerating voltage of 80 kV to reduce radiation damage.

**AFM and Spectroscopy Characterization:** The AFM characterization was carried out on a Dimension 3100 instrument, commercially available from Veeco Instruments Inc. PL and Raman spectra were taken on a Horiba Jobin-Yvon HR800 system and a Witec Alpha300-Confocal Raman Microscope. The laser excitation wavelength for the PL and Raman measurements was typically 532.5 nm. The laser power on the sample was  $\approx 0.1$  mW. A  $100\times$  objective was used to focus the laser beam. The spectral parameters were obtained by fitting the peaks using Lorentzian/Gaussian mixed functions as appropriate. For Raman and PL mapping, the scan step is  $0.8\ \mu\text{m}$  on the Horiba Jobin-Yvon HR800 system and  $0.3\ \mu\text{m}$  on the Witec Alpha300-Confocal Raman Microscope.

**Device Fabrication and Measurement:** The MoS<sub>2</sub>–graphene heterostructures were first transferred onto the  $300\ \text{nm SiO}_2/\text{Si}$  substrates through the PMMA transfer technique as mentioned earlier. E-beam lithography (EBL), e-beam evaporation followed by a lift-off process were used to deposit  $20\ \text{nm Au}$  as the Ohmic contacts. Another round of EBL and reactive ion etching with oxygen plasma were used to define the channel area. For top-gated devices,  $35\ \text{nm Al}_2\text{O}_3$  was deposited through atomic layer deposition as the gate dielectric, followed by an e-beam evaporation of  $30\ \text{nm Pd}$  as the gate electrodes. The transport measurements were carried out in vacuum ( $\approx 10^{-5}$  Torr) using a semiconductor parameter analyzer (Agilent 4155C) and a cryogenic probe station (Lakeshore).

## Supporting Information

Supporting Information is available from the Wiley Online Library or from the author.

## Acknowledgements

X.L. and Y.L. contributed equally to this work. This work was supported by the U.S. Army Research Office through the MIT Institute for Soldier Nanotechnologies, under Award No. 023674. X.L., Y.L., and M.D. acknowledge partial support from the National Science Foundation (NSF) under Award No. NSF/DMR 1004147. X.L. and M.D. acknowledge partial support from the Department of Energy (DOE) under Award No. DE-SC0001299. Y.L. and T.P. acknowledge the support from the Office of Naval Research (ONR) Presidential Early Career Awards for Scientists and Engineers (PECASE) program under Award No. 021302-001. Y.Z. and L.W. acknowledge the support from DOE-Basic Energy Sciences (BES) / Materials Science and Engineering (MSE) division under Contract No. DE-AC02-98CH10886. Y.-H.L. acknowledges partial support from the Ministry of Science and Technology of the Republic of China (MOST 103-2112-M-007-001-MY3). This work was performed in part at the Center for Nanoscale Systems (CNS), a member of the National Nanotechnology Infrastructure Network (NNIN), which is supported by the National Science Foundation under NSF Award No. ECS-0335765. CNS is part of Harvard University. Device fabrications were made in MIT Microsystems

Technology Laboratories (MTL). TEM characterization was carried out at Brookhaven National Laboratory and at MIT Center for Material Science and Engineering (CMSE). The authors thank Xiang Zhou, Xiaoting Jia, Albert D. Liao, Xiang Ji, and Edbert J. Sie for their help and advice.

Received: October 14, 2015

Revised: November 14, 2015

Published online: January 27, 2016

- [1] International Technology Roadmap for Semiconductors, <http://www.itrs.net/>, accessed: January 2015.
- [2] L. Yu, *M.Sc. Thesis*, Massachusetts Institute of Technology, Cambridge, MA, USA **2013**.
- [3] A. Nathan, A. Ahnood, M. T. Cole, Sungsik Lee, Y. Suzuki, P. Hiralal, F. Bonaccorso, T. Hasan, L. Garcia-Gancedo, A. Dyadyusha, S. Haque, P. Andrew, S. Hofmann, J. Moultrie, Daping Chu, A. J. Flewitt, A. C. Ferrari, M. J. Kelly, J. Robertson, G. A. J. Amaratunga, W. I. Milne, *Proc. IEEE* **2012**, *100*, 1486.
- [4] K. Roy, M. Padmanabhan, S. Goswami, T. P. Sai, G. Ramalingam, S. Raghavan, A. Ghosh, *Nat. Nanotechnol.* **2013**, *8*, 826.
- [5] W. J. Yu, Z. Li, H. Zhou, Y. Chen, Y. Wang, Y. Huang, X. Duan, *Nat. Mater.* **2012**, *12*, 246.
- [6] C. R. Dean, A. F. Young, I. Meric, C. Lee, L. Wang, S. Sorgenfrei, K. Watanabe, T. Taniguchi, P. Kim, K. L. Shepard, J. Hone, *Nat. Nanotechnol.* **2010**, *5*, 722.
- [7] Z. Liu, L. Ma, G. Shi, W. Zhou, Y. Gong, S. Lei, X. Yang, J. Zhang, J. Yu, K. P. Hackenberg, A. Babakhani, J.-C. Idrobo, R. Vajtai, J. Lou, P. M. Ajayan, *Nat. Nanotechnol.* **2013**, *8*, 119.
- [8] W. J. Yu, Y. Liu, H. Zhou, A. Yin, Z. Li, Y. Huang, X. Duan, *Nat. Nanotechnol.* **2013**, *8*, 952.
- [9] L. Britnell, R. M. Ribeiro, A. Eckmann, R. Jalil, B. D. Belle, A. Mishchenko, Y.-J. Kim, R. V. Gorbachev, T. Georgiou, S. V. Morozov, A. N. Grigorenko, A. K. Geim, C. Casiraghi, A. H. C. Neto, K. S. Novoselov, *Science* **2013**, *340*, 1311.
- [10] M.-Y. Li, Y. Shi, C.-C. Cheng, L.-S. Lu, Y.-C. Lin, H.-L. Tang, M.-L. Tsai, C.-W. Chu, K.-H. Wei, J.-H. He, W.-H. Chang, K. Suenaga, L.-J. Li, *Science* **2015**, *349*, 524.
- [11] M. P. Levendorf, C.-J. Kim, L. Brown, P. Y. Huang, R. W. Havener, D. A. Muller, J. Park, *Nature* **2012**, *488*, 627.
- [12] L. Liu, J. Park, D. A. Siegel, K. F. McCarty, K. W. Clark, W. Deng, L. Basile, J. C. Idrobo, A.-P. Li, G. Gu, *Science* **2014**, *343*, 163.
- [13] X. Duan, C. Wang, J. C. Shaw, R. Cheng, Y. Chen, H. Li, X. Wu, Y. Tang, Q. Zhang, A. Pan, J. Jiang, R. Yu, Y. Huang, X. Duan, *Nat. Nanotechnol.* **2014**, *9*, 1024.
- [14] C. Huang, S. Wu, A. M. Sanchez, J. J. P. Peters, R. Beanland, J. S. Ross, P. Rivera, W. Yao, D. H. Cobden, X. Xu, *Nat. Mater.* **2014**, *13*, 1096.
- [15] Y. Gong, J. Lin, X. Wang, G. Shi, S. Lei, Z. Lin, X. Zou, G. Ye, R. Vajtai, B. I. Yakobson, H. Terrones, M. Terrones, B. K. Tay, J. Lou, S. T. Pantelides, Z. Liu, W. Zhou, P. M. Ajayan, *Nat. Mater.* **2014**, *13*, 1135.
- [16] X.-Q. Zhang, C.-H. Lin, Y.-W. Tseng, K.-H. Huang, Y.-H. Lee, *Nano Lett.* **2015**, *15*, 410.
- [17] X. Ling, Y.-H. Lee, Y. Lin, W. Fang, L. Yu, M. S. Dresselhaus, J. Kong, *Nano Lett.* **2014**, *14*, 464.
- [18] S. Wang, Y. Zhang, N. Abidi, L. Cabrales, *Langmuir* **2009**, *25*, 11078.
- [19] P. K. Chow, E. Singh, B. C. Viana, J. Gao, J. Luo, J. Li, Z. Lin, A. L. Elías, Y. Shi, Z. Wang, M. Terrones, N. Koratkar, *ACS Nano* **2015**, *9*, 3023.

- [20] A. N. Enyashin, M. Bar-Sadan, L. Houben, G. Seifert, *J. Phys. Chem. C* **2013**, *117*, 10842.
- [21] A. M. van der Zande, P. Y. Huang, D. A. Chenet, T. C. Berkelbach, Y. You, G.-H. Lee, T. F. Heinz, D. R. Reichman, D. A. Muller, J. C. Hone, *Nat. Mater.* **2013**, *12*, 554.
- [22] S. M. Sze, K. K. Ng, *Physics of Semiconductor Devices*, John Wiley & Sons, Inc., Hoboken, NJ, USA, **2006**.
- [23] J. Y. Kwak, J. Hwang, B. Calderon, H. Alsalman, N. Munoz, B. Schutter, M. G. Spencer, *Nano Lett.* **2014**, *14*, 4511.
- [24] L. Britnell, R. V. Gorbachev, R. Jalil, B. D. Belle, F. Schedin, A. Mishchenko, T. Georgiou, M. I. Katsnelson, L. Eaves, S. V. Morozov, N. M. R. Peres, J. Leist, A. K. Geim, K. S. Novoselov, L. A. Ponomarenko, *Science* **2012**, *335*, 947.
- [25] L. Yu, Y.-H. Lee, X. Ling, E. J. G. Santos, Y. C. Shin, Y. Lin, M. Dubey, E. Kaxiras, J. Kong, H. Wang, T. Palacios, *Nano Lett.* **2014**, *14*, 3055.
- [26] Y.-C. Lin, C.-Y. S. Chang, R. K. Ghosh, J. Li, H. Zhu, R. Addou, B. Diaconescu, T. Ohta, X. Peng, N. Lu, M. J. Kim, J. T. Robinson, R. M. Wallace, T. S. Mayer, S. Datta, L.-J. Li, J. A. Robinson, *Nano Lett.* **2014**, *14*, 6936.
- [27] L. Wang, I. Meric, P. Y. Huang, Q. Gao, Y. Gao, H. Tran, T. Taniguchi, K. Watanabe, L. M. Campos, D. A. Muller, J. Guo, P. Kim, J. Hone, K. L. Shepard, C. R. Dean, *Science* **2013**, *342*, 614.
- [28] H. Wang, L. Yu, Y.-H. Lee, Y. Shi, A. Hsu, M. L. Chin, L.-J. Li, M. Dubey, J. Kong, T. Palacios, *Nano Lett.* **2012**, *12*, 4674.